

On the onset of low-Prandtl-number convection in rotating spherical shells: non-slip boundary conditions

MARTA NET, FERRAN GARCIA AND JUAN SÁNCHEZ

Departament de Física Aplicada, Universitat Politècnica de Catalunya
Jordi Girona Salgado s/n. Campus Nord. Mòdul B4, 08034 Barcelona, Spain
marta@fa.upc.edu; sanchez@fa.upc.edu

(Received 18 December 2006 and in revised form 15 January 2008)

Accurate numerical computations of the onset of thermal convection in wide rotating spherical shells are presented. Low-Prandtl-number (σ) fluids, and non-slip boundary conditions are considered. It is shown that at small Ekman numbers (E), and very low σ values, the well-known equatorially trapped patterns of convection are superseded by multicellular outer-equatorially-attached modes. As a result, the convection spreads to higher latitudes affecting the body of the fluid, and increasing the internal viscous dissipation. Then, from $E < 10^{-5}$, the critical Rayleigh number (R_c) fulfils a power-law dependence $R_c \sim E^{-4/3}$, as happens for moderate and high Prandtl numbers. However, the critical precession frequency ($|\omega_c|$) and the critical azimuthal wavenumber (m_c) increase discontinuously, jumping when there is a change of the radial and latitudinal structure of the preferred eigenfunction. In addition, the transition between spiralling columnar (SC), and outer-equatorially-attached (OEA) modes in the (σ, E) -space is studied. The evolution of the instability mechanisms with the parameters prevents multicellular modes being selected from $\sigma \gtrsim 0.023$. As a result, and in agreement with other authors, the spiralling columnar patterns of convection are already preferred at the Prandtl number of the liquid metals. It is also found that, out of the rapidly rotating limit, the prograde antisymmetric (with respect to the equator) modes of small m_c can be preferred at the onset of the primary instability.

1. Introduction

The first attempts to find the asymptotic dependence of the non-axisymmetric onset of thermal convection in self-gravitating and internally heated fluid spheres were by Roberts (1968), and Busse (1970). In these early papers the scaling laws $R_c \sim E^{-4/3}$, $|\omega_c| \sim E^{-2/3}$, $m_c \sim E^{-1/3}$, the symmetry, and the azimuthal drifting of the marginal columnar modes of convection at large rotation rates were established. These modes were localized inside a cylinder centred at a critical interior radius. Later, the non-local perturbation analysis of Soward (1977) showed that small disturbances, at values of the Rayleigh number just above R_c given by the Roberts–Busse theory, decay exponentially as $t \rightarrow \infty$. The weak point of their analysis comes from using a local theory that neglects the dependence of the boundary inclination on the distance to the axis of rotation.

The numerical calculations of Zhang & Busse (1987), and Zhang (1992) revealed that, in rapidly rotating spherical shells, the preferred modes of convection are strongly

dependent on the Prandtl and Ekman numbers. At fast rotation rates, and moderate and large Prandtl numbers, they are thermal Rossby waves in the form of spiralling columns, while, at low Prandtl numbers, they are waves attached to the equator (equatorially trapped waves).

A revised asymptotic theory for the spiralling columnar convection was proposed by Yano (1992). Following the guidelines of Soward (1977), he improved the critical parameters for $\sigma > 0.1$ by extending the solution of Roberts (1968), and Busse (1970) onto a complex plane of the radial coordinate of the point where the convection amplitude attains its maximum, but maintaining the limit of small inclination of the boundaries. The projection of the solution onto the real axis gives the inclination of the columns with respect to the radial direction. His calculations agree well with the numerical results. Jones, Soward & Mussa (2000) have determined the leading-order value of R_c , and the first-order correction for the columnar convection in spheres with internal heating, and stress-free boundary conditions. They have generalized the work of Yano (1992) by considering the full spherical problem. For the same problem, Busse & Simitev (2004) have found explicit expressions for the dependence of R_c on m_c . On the other hand, Dormy *et al.* (2004) have completed the asymptotic theory for the onset of columnar convection in spherical shells. The differential heating problem, for which there are no heat sources in the fluid, is also studied. Then, the critical mode of convection localizes around the inner radius because, according to the authors, the conduction temperature gradient ($\propto r^{-2}$) decreases very rapidly by increasing r . In this work, the corrections due to Ekman suction are included.

In the 1990s, many theoretical and numerical papers were devoted to the study of the spiralling columnar type of convection, mainly with stress-free boundary conditions, since it is relevant to astrophysical problems. The dependence of R_c , ω_c and m_c on E and σ , and the influence of the Ekman boundary layers on the onset of convection in spherical shells were studied by Zhang & Jones (1993). For fluids of $\sigma \geq O(1)$, their numerical results show that the extra dissipation in the Ekman boundary layers generated near the rigid boundaries destabilizes the flow, and also reduces $|\omega_c|$, and m_c . However, for $\sigma < O(1)$, and moderate E , the thermal dissipation dominates over the viscous dissipation, and the boundary layers stabilize the flow.

Low-Prandtl-number problems are important in magnetohydrodynamics since they model planetary metallic cores. The importance of equatorial drifts in the Earth's core was stated by Finlay & Jackson (2003). They showed a westward drift of the equatorial patches of the radial magnetic field from observations of the magnetic field flux over 400 years. This phenomenon may be due to either waves or advection by the underlying flow. The latest estimations of the thermal and magnetic Prandtl numbers for the Earth's outer core are $\sigma \approx 0.1$ and 10^{-6} , respectively. They are based on the value of the viscosity determined by Wijs *et al.* (1998), and on the electrical resistivity determined by Secco & Schloessin (1989), at the physical pressure and temperature conditions of the Earth's outer core. The study of thermal convection with liquid metals in these conditions is very difficult. The numerical computations require very high resolutions to approach the extremely low Ekman numbers of the cores, and to solve the thin Ekman boundary layers near the rigid boundaries. For this reason, there have been very few attempts to compute the marginal modes in this range of parameters. Frequently, as in Pino, Mercader & Net (2000), Plaut & Busse (2005), and Gillet *et al.* (2007), a quasi-geostrophic model is used to approximate the real problem.

According to Zhang (1993, 1994), the equatorially trapped modes are quasi-inertial waves, i.e. at leading order they are solutions of the Poincaré equation.

Moreover, Ardes, Busse & Wicht (1997) found that, at moderate rotation rates and stress-free boundary conditions, the dominant modes remain attached to the outer equator, but can be multicellular before the transition to spiralling columns at low Ekman numbers. They supplied a sketch of this transition in the (σ, E) -plane. In the work of Plaut & Busse (2005), valid for $E \lesssim \sigma$, it is seen that in cylindrical annuli with curved lids the critical modes at small σ are also quasi-inertial and multicellular. In addition, they have demonstrated by a perturbation analysis, that R_c decreases when the number of vortices of the streamfunction in the radial direction increases, because it depends on a balance between dissipation and buoyancy. The increase of power consumed by viscous dissipation is overcome by a much more efficient release of power developed by the buoyancy forces. This effect is due essentially to the fall of the precession frequency of the wave when the number of cells increases.

There are no accurate experiments on the onset of convection using low-Prandtl-number fluids. The only experimental study is that of Jaletzky (1999), although the apparatus is a cylindrical annulus of conical lids. By using mercury ($\sigma = 0.025$), he measured low-frequency rotating waves for Rayleigh numbers of order E^{-2} . However, it is important to notice that, in the nonlinear regime, Aubert *et al.* (2001) and Gillet *et al.* (2007) have found experimental retrograde zonal flows (generated by Reynolds stresses) storing most of the kinetic energy of the fluid.

The first study of the asymptotic dependence of R_c and ω_c in the small-Ekman-number limit, for the equatorially trapped convection in a self-gravitating fluid sphere, including solutions of the spherical boundary layer, is that of Zhang (1995). His perturbation analysis is valid only for very low Prandtl numbers, namely $\sigma \ll Em^{5/2}$. For small but finite σ , no simple power-law dependence can be derived from this perturbation theory. Zhang & Liao (2004), and Zhang, Liao & Busse (2007) have proposed a new method for the study of the asymptotic solutions in a rapidly rotating sphere, which does not assume any asymptotic scaling for $E \ll 1$. Then it is valid for $0 \leq \sigma/E < \infty$, i.e. it also includes moderately small and high Prandtl numbers. The main contribution of these papers is to unify the inertial-oscillation and the convective instability problems for both stress-free and non-slip boundary conditions. The eigenfunctions are written either as a single or as a superposition of quasi-geostrophic inertial modes, and it is shown that the viscous coupling of these modes causes the spiralling structure of convection. The analytical results are compared with those obtained from a numerical code for a wide spherical shell displaying a good agreement in any considered case.

This paper seeks to help to understand the onset of thermal convection at small Prandtl numbers between rigid spherical boundaries. Specifically, the dependence of R_c , ω_c and m_c on E and σ , and the features of the preferred modes of convection in the parameter space are studied. The small value of the radius ratio $\eta = 0.2$ will be maintained in the paper for three reasons. Until now, the known preferred modes of convection were spiralling columnar or equatorially attached for any η value, so $\eta = 0.2$ facilitates the calculations because the number of relevant marginal stability curves is small, and they are much more separated than for higher η values. In the second place, it concerns geophysical applications, because the Earth's outer core is a wide spherical shell, so the study is restricted to $0.005 \leq \sigma \leq 0.1$. Finally, it facilitates comparison with preceding papers.

In §2, we introduce the formulation of the problem, and the numerical method used to find the leading spectra of the linearized equations. We also include some of the tests made in order to check our new computational code. In §3, the marginal stability curves as a function of E and σ , and the structure of the preferred patterns of

convection are analysed. A comparison between these results and previous asymptotic and numerical analysis, in the low-Prandtl-number limit, is also established. Finally, in §4, the paper ends with some brief comments on the results obtained.

2. Mathematical model and numerical method

A spherical shell rotating about an axis of symmetry with constant angular velocity $\boldsymbol{\Omega} = \Omega \mathbf{k}$, and radial gravity $\mathbf{g} = -\gamma \mathbf{r}$, where γ is a constant, and \mathbf{r} the position vector, is considered. The gap width is $d \equiv r_o - r_i$, where r_i and r_o are the inner and outer radii. We use the same formulation of the problem as in Simitev & Busse (2003), which allows us to study internal and differential heating at the same time. The non-dimensional units are d for the distance, $v^2/\gamma\alpha d^4$ for the temperature, and d^2/ν for the time; ν being the kinematic viscosity, and α the thermal expansion coefficient.

The velocity field is written in terms of toroidal and poloidal potentials

$$\mathbf{v} = \nabla \times (\Psi \mathbf{r}) + \nabla \times \nabla \times (\Phi \mathbf{r}), \quad (2.1)$$

consequently, the linearized equations for both potentials, and the temperature perturbation Θ from the conduction state ($\mathbf{v} = \mathbf{0}$, $T = T_c(r)$), with $r = \|\mathbf{r}\|_2$, are

$$[(\partial_t - \nabla^2)L_2 - 2E^{-1}\partial_\varphi]\Psi = -2E^{-1}Q\Phi, \quad (2.2)$$

$$[(\partial_t - \nabla^2)L_2 - 2E^{-1}\partial_\varphi]\nabla^2\Phi + L_2\Theta = 2E^{-1}Q\Psi, \quad (2.3)$$

$$(\sigma\partial_t - \nabla^2)\Theta - (R_i + R_e\eta(1-\eta)^{-2}r^{-3})L_2\Phi = 0. \quad (2.4)$$

The parameters of the problem are the internal R_i , and external R_e , Rayleigh numbers, the Prandtl number σ , the Ekman number E , and the radius ratio η ,

$$R_i = \frac{\gamma\alpha q d^6}{3c_p\kappa^2\nu}, \quad R_e = \frac{\gamma\alpha\Delta T d^4}{\kappa\nu}, \quad E = \frac{\nu}{\Omega d^2}, \quad \sigma = \frac{\nu}{\kappa}, \quad \eta = \frac{r_i}{r_o}, \quad (2.5)$$

κ being the thermal diffusivity, c_p the specific heat at constant pressure, q the rate of heat due to internal sources per unit volume, and ΔT the difference of temperature between the inner and outer boundaries due only to differential heating. The operators L_2 and Q are defined by $L_2 \equiv -r^2\nabla^2 + \partial_r(r^2\partial_r)$, $Q \equiv r \cos\theta\nabla^2 - (L_2 + r\partial_r)(\cos\theta\partial_r - r^{-1}\sin\theta\partial_\theta)$, (r, θ, φ) being the spherical coordinates, with θ measuring the colatitude. In non-dimensional units, the conduction state reads

$$T_c(r) = T_0 - (R_i/2\sigma)r^2 + (R_e\eta/\sigma(1-\eta)^2)/r. \quad (2.6)$$

Non-slip perfect thermally conducting boundaries

$$\Phi = \partial_r\Phi = \Psi = \Theta = 0 \quad (2.7)$$

are used, but for testing purposes also stress-free $\Phi = \partial_{rr}^2\Phi = \partial_r(\Psi/r) = \Theta = 0$ boundary conditions are implemented.

The system is $\mathcal{SO}(2) \times \mathcal{L}_2$ -equivariant, $\mathcal{SO}(2)$ generated by azimuthal rotations, and \mathcal{L}_2 by reflections with respect to the equatorial plane, i.e. the actions

$$\left. \begin{aligned} \varphi &\rightarrow \varphi + \varphi_o, & u &\rightarrow u, \\ \theta &\rightarrow \pi - \theta, & u &\rightarrow \zeta u, \end{aligned} \right\} \quad (2.8)$$

with $u = (\Psi, \Phi, \Theta)$, and $\zeta u = (-\Psi, \Phi, \Theta)$, leave the system invariant. In terms of the velocity field, the same holds with $u = (v_r, v_\theta, v_\varphi, \Theta)$ and $\zeta u = (v_r, -v_\theta, v_\varphi, \Theta)$.

The equations for $X = (\Phi, \Psi, \Theta)$ are solved by expanding the eigenfunctions in spherical harmonic series up to degree L , namely

$$X(t, r, \theta, \varphi) = \sum_{l=0}^L \sum_{m=-l}^l X_l^m(r, t) Y_l^m(\theta, \varphi), \quad (2.9)$$

with $Y_l^m(\theta, \varphi) = P_l^m(\cos \theta) e^{im\varphi}$, and P_l^m being the normalized associated Legendre functions of degree l and order m . In the radial direction, a collocation method on a Gauss–Lobatto mesh is employed.

In order to find the critical parameters we use a new computational code, which allows us to find the leading eigenvalues with a good resolution by means of an iterative method. The linearized equations (2.2)–(2.4), (2.7) are separated into their azimuthal Fourier coefficients. Let the equations for a given azimuthal mode m be written as

$$\dot{\mathbf{x}}_m = \mathcal{A}_m \mathbf{x}_m, \quad (2.10)$$

where \mathbf{x}_m are all the values at the collocation mesh of the amplitudes of the variables in spherical harmonics of order m . We compute the eigenvalues of \mathcal{A}_m by evolving (2.10) a time t . Its solution with initial condition \mathbf{x}_m^0 is $\exp(t\mathcal{A}_m)\mathbf{x}_m^0$. The eigenvalues μ of the linear map $\exp(t\mathcal{A}_m)$ are related to the eigenvalues λ of \mathcal{A}_m by $\mu = \exp(t\lambda)$. This transformation maps eigenvalues of maximum real part of \mathcal{A}_m to multipliers of largest modulus of $\exp(t\mathcal{A}_m)$. To find the latter we employ subspace iteration or Arnoldi algorithms (see Lehoucq, Sorensen & Yang 1998). The integration of (2.10) is performed by a multi-step BDF-extrapolation formulae (BDF meaning backward differentiation formulae), with initial conditions obtained by a Runge–Kutta method. It is important to notice that an explicit treatment of the term in Q allows us to decouple the left-hand sides of (2.2)–(2.4) for each degree l . The time interval t is selected to be as short as possible to reduce the cost of the evaluation of $\exp(t\mathcal{A}_m)\mathbf{x}_m^0$, but large enough to separate the eigenvalues to make their convergence fast.

The onset of convection breaks the axisymmetry of the conduction state. Then, according to Ecke, Zhong & Knobloch (1992), it is a Hopf bifurcation giving rise to a wave travelling in the azimuthal direction. Typically, the critical solutions maintain the \mathcal{L}_2 symmetry with respect to the equatorial plane, i.e. they are symmetric with respect to the equator. This implies that only associated Legendre functions with odd $(m+l)$ for Ψ , and even for Φ and Θ contribute to the linear problem. Then, the number of unknowns can be halved if needed. However, it will be seen that at low rotation rates, antisymmetric modes can also be selected at onset. Moreover, from moderate rotation rates, the axisymmetric ($m=0$) modes of convection are waves travelling from the equator or mid-latitudes to the poles. Although they are non-preferred linearly, nonlinear interactions involving these modes could give rise to waves of this type at higher Rayleigh numbers.

Table 1 shows the convergence of the numerical method by increasing the number of radial points N_r , and the maximal degree L of the associated Legendre functions, for $E = 3.16 \times 10^{-6}$. All the results of table 1 correspond to a fourth-order time-integration method. The tolerances required are kept at each run of the code. However, we have checked, by changing the time step and the order of the method, that we do not introduce numerical instabilities that could lead to erroneous critical parameters. In

$N_r \times L$	R_{i_c}	$-\omega_c$
40×65	8 836 856.9	16 513.198
40×85	8 850 865.2	16 513.533
50×85	8 644 084.1	16 545.639
50×100	8 645 078.5	16 545.794
60×85	8 627 974.3	16 547.513
60×100	8 629 021.4	16 547.655
70×85	8 627 670.2	16 547.753

TABLE 1. Convergence of the iterative method for $\eta = 0.2$, $\sigma = 0.005$, $E = 3.16 \times 10^{-6}$, $m = 5$ and $R_e = 0$, with a fourth-order time integrator.

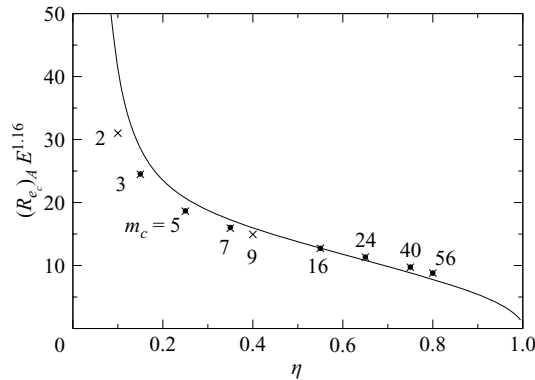


FIGURE 1. Critical Rayleigh number $(R_{e_c})_A E^{1.16}$ versus the radius ratio η for $\sigma = 1$, and $E = 10^{-4}$. The integer numbers denote the critical azimuthal wavenumber, m_c , of the preferred modes of convection for each η computed.

the table, R_{i_c} means the critical internal Rayleigh number. The negative frequencies give positive drifting velocities $c = -\omega_c/m$, i.e. in this case, the waves precess in the prograde direction.

We have also checked our code working with non-slip boundary conditions with Al-Shamali, Heimpel & Arnou (2004) for differential heating, with Zhang (1995) for internal heating, with Li *et al.* (2005) for a non-rotating shell, also with internal heating, and finally, with Simitev & Busse (2003) for internal heating and stress-free boundary conditions. The satisfactory results of the first comparison are plotted in figure 1, for various η values. The critical Rayleigh number $(R_{e_c})_A$ used in Al-Shamali *et al.* (2004) is related to ours by $(R_{e_c})_A = R_{e_c}/(1 - \eta)$. The full circles and crosses correspond to their and our numerical results, respectively, and the solid line is their fitting to the solutions. Our results also agree very well with those presented in the first figure of Li *et al.* (2005) with tiny differences of less than 0.06 % for the two η of that figure. We do not know exactly the resolution employed in Simitev & Busse (2003), but, the differences are less than 1.3 % in R_{i_c} , and 0.2 % in ω_c for $\sigma = 0.025$. However, we have found discrepancies greater than 13 % in R_{i_c} with Zhang (1995), which will be explained below.

Hereinafter only $\eta = 0.2$, and internal heating is considered, so $R_e = 0$, and $R = R_i$ is defined.

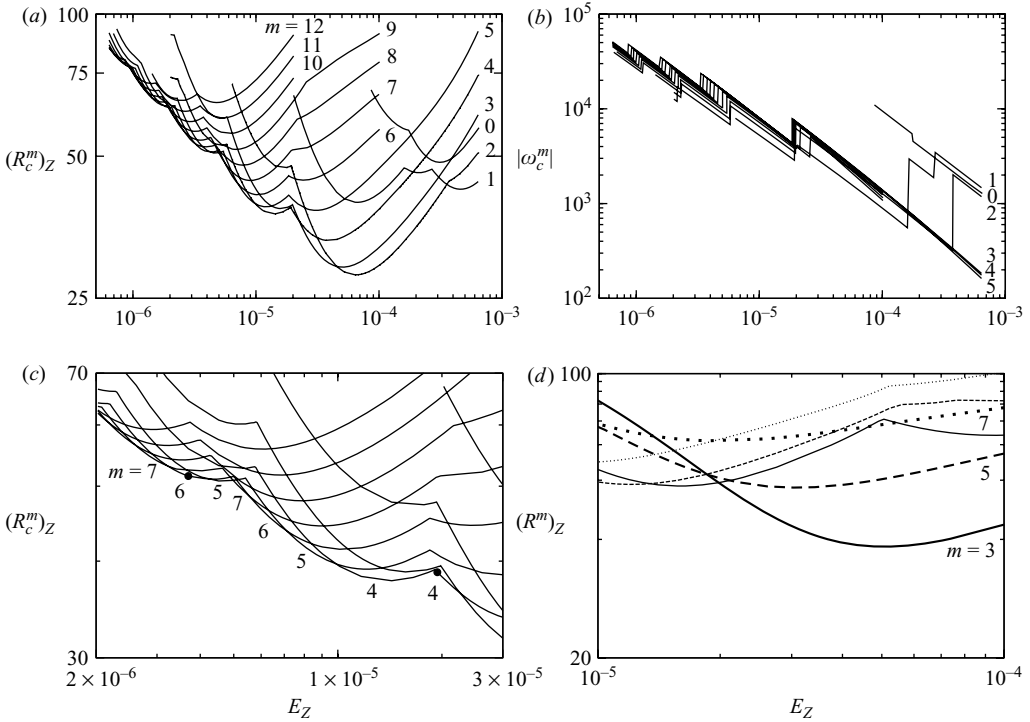


FIGURE 2. (a) The critical Rayleigh number $(R_c^m)_Z$, and (b) the critical precession frequency $|\omega_c^m|$, of each critical mode with azimuthal wavenumber m , plotted versus the Ekman number E_Z for $\sigma = 0.005$. (c) Detail of (a) showing pairs of different preferred modes with the same wavenumber m . The full circles indicate the parameters of figures 3 and 4. (d) The two lowest marginal stability curves for $m = 3$ (thick and thin solid lines), $m = 5$ (thick and thin dashed lines), and $m = 7$ (thick and thin dotted lines) azimuthal modes. The $m = 3, 5, 7$ thick lines were also calculated by Zhang (1995).

3. Numerical results

3.1. Dependence of very low Prandtl number flows on the Ekman number

First of all, the stability of the conduction state is studied for $\sigma = 0.005$, the very low Prandtl number case computed in Zhang (1995). A mesh $N_r \times L = 50 \times 85$ is used, because it guarantees relative errors below 0.2% in the critical Rayleigh numbers at least up to $E = 3.16 \times 10^{-6}$ (see table 1), and minimizes the computing time. Figure 2(a–c) shows the critical Rayleigh number R_c^m , and the critical precession frequency $|\omega_c^m|$ versus E , for each neutral stability curve of azimuthal wavenumber m . In order to facilitate the comparison with Zhang, and to show the change of modes, E and R_c^m are rescaled in the figure in accordance with Zhang (Z) units. The relations are $E_Z = E(1 - \eta)^2$ and $(R_c^m)_Z = R_c^m E / (1 - \eta)^4$.

The cusps in each curve of figure 2(a) and its enlargement figure 2(c) indicate crossings between curves of the same wavenumber m . In figure 2(a), for $E_Z > 3.6 \times 10^{-4}$ the preferred $m = 1$ patterns of convection are symmetric retrograde ($\omega_c > 0$) body modes, in the sense that they fill the shell up to the polar regions. Then, they are superseded by prograde waves ($\omega_c^m < 0$) of $m = 2, 3, 4$, whose shape is weakly influenced by rotation. When the Ekman number is decreased, they become more and more confined to the equatorial region, and at $E_Z \lesssim 3 \times 10^{-5}$ these critical

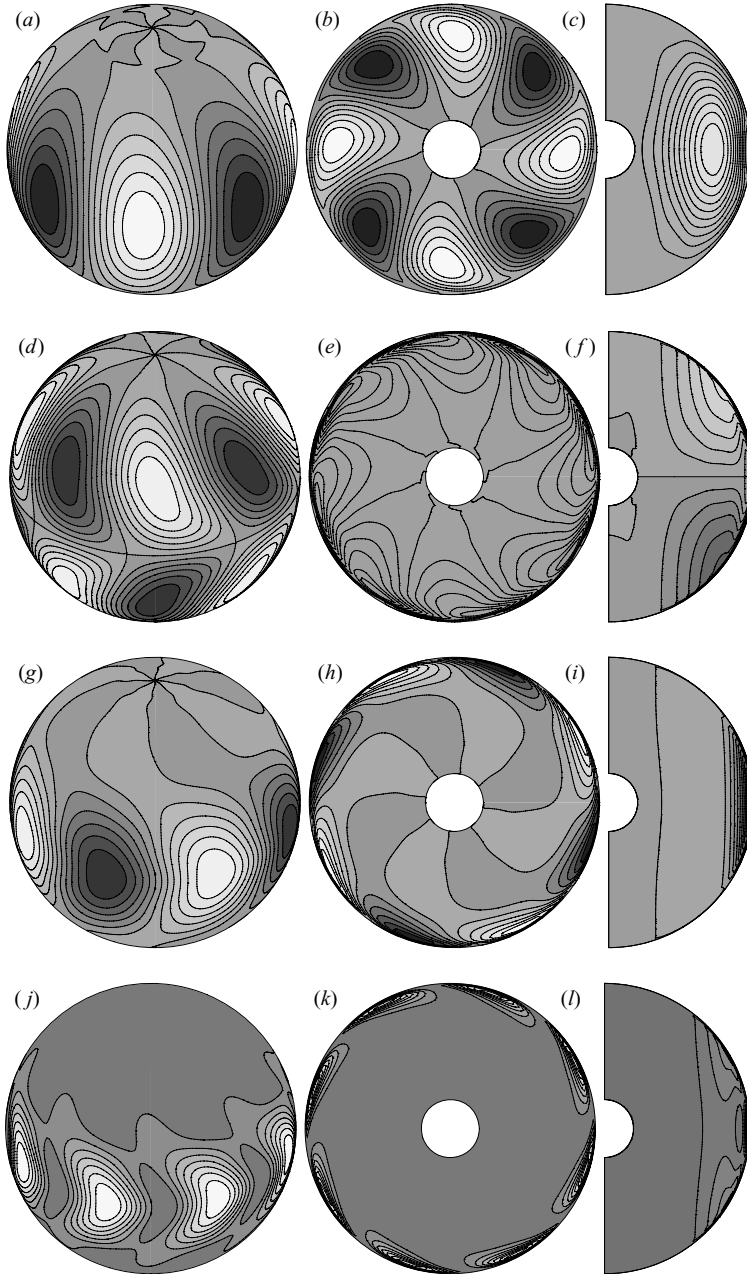


FIGURE 3. The preferred equatorially trapped mode of convection with azimuthal wavenumber $m = 4$, plotted at $E_Z = 1.92 \times 10^{-5}$ for $\sigma = 0.005$. Contour plots of the radial velocity field (a) on a sphere, (b) on the equatorial plane, and (c) on a meridional section. (d–f) As (a–c) for the colatitudinal velocity. (g–i) As (a–c) for the azimuthal velocity. (j–l) As (a–c) for the kinetic energy density.

eigenfunctions can be recognized clearly as the equatorially trapped modes (see figure 3) described for the first time in Zhang & Busse (1987). From this point, the crossings of the curves of the same m produce decreases of m_c , which lead to critical eigenfunctions with the same m_c , and relative extrema inside the arms of the spirals

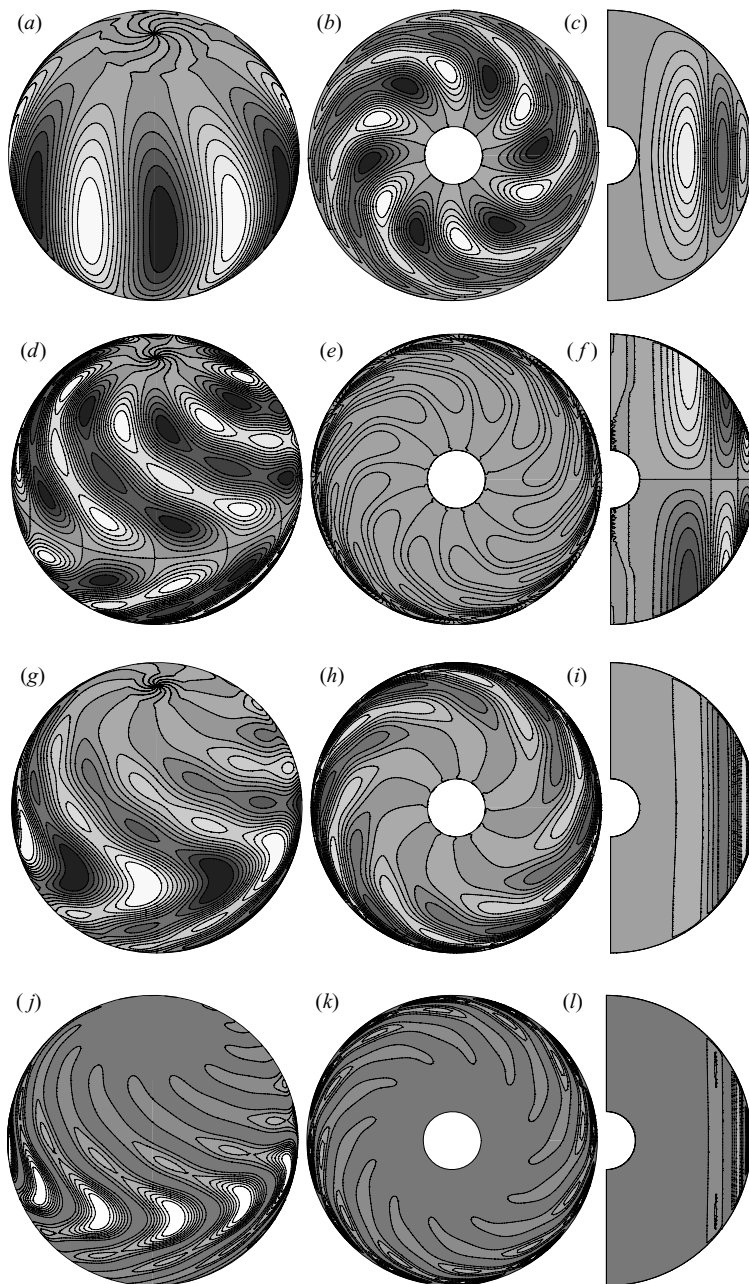


FIGURE 4. The preferred tri-cellular mode of convection with azimuthal wavenumber $m = 6$, plotted at $E_Z = 3.69 \times 10^{-6}$ for $\sigma = 0.005$. Same contour plots as in figure 3.

(see figure 4). The components v_r and v_ϕ have extrema on the equatorial plane, and v_θ and v_ϕ on spherical projections very close to the outer boundary. So, these eigenfunctions display multicellular patterns of convection. We will refer to their shape on the equatorial plane as the *radial structure*, that on spherical projections as the *latitudinal structure*, and the local vortices on these projections as *latitudinal cells*. In figure 2(c), modes with $m = 5, 6, 7$ dominate successively twice in a short

range of E_Z . In any case, the main contribution to the latitudinal structure of the dominant modes corresponds to the associated Legendre functions with $l = m_c$ for Φ and Θ , and $l = m_c + 1$ for Ψ . The only difference seems to be the relative weight of the associated Legendre functions of higher degree.

Figure 2(b) shows $|\omega_c|$ in a logarithmic scale versus E_Z . The jumps also indicate the changes between radial and latitudinal patterns of convection, which can maintain the azimuthal wavenumber. When E decreases, the waves drift more slowly after every jump. Moreover, under the influence of rotation, the vortices tend to spiral eastward, and to split, forming cells attached to the outer boundary of the fluid. We will employ the term outer equatorially attached (OEA) modes to describe both the equatorially trapped patterns (mono-cellular) and the multicellular equatorially attached patterns, to distinguish them from the well-known spiralling columnar (SC) modes preferred at moderate and large Prandtl numbers.

In Yano (1992), the localized columnar convection is explained from the dispersion relation of the wave. There, it is seen that the existence of a columnar mode requires a strong buoyancy force counterbalanced by the kinematic diffusivity, and then the thermal diffusivity acts to isolate the columns. However, without an effective kinematic diffusivity ($\sigma < O(1)$), the pattern becomes a spiralling column. We have checked that when the multicellular modes become selected, the viscous dissipation in the body of the fluid increases, but the buoyancy force decreases significantly, so for these solutions the preceding balance is not fulfilled. Nevertheless, our result agree with the conclusions of Zhang *et al.* (2007). They demonstrate that the tendency of the multicellular modes to spiralling is due merely to the viscous coupling of different quasi-geostrophic inertial waves.

Figure 2(d) shows the two lowest marginal stability curves for $m = 3, 5, 7$, in the range of E_Z of figure 1(b) of Zhang (1995). Zhang's figure 1(b) illustrated the comparison between the $m = 3, 5, 7$ curves found in his numerical analysis for $\eta = 0.2$ with those obtained by a perturbation method, but for a full sphere. Our thick marginal curves agree very well with those found by Zhang, but they do not give R_c^m in the full interval. As can be seen in figure 2(d), from $E_Z < 1.98 \times 10^{-5}$ they are superseded by the thin lines (not found before), which correspond to multicellular modes. Namely, in the spherical shell, the thick curves, which correspond to equatorially trapped modes of one cell, give the correct R_c^m only down to $E_Z = 1.98 \times 10^{-5}$. From this point, multicellular OEA modes become preferred. This explains the important differences we found in R_c^m when comparing both results at high rotation rates in order to check our code.

Figures 3 and 4 show the contour plots of two preferred eigenfunctions. The first is an $m = 4$ equatorially trapped mode preferred at moderate E_Z , and the second an $m = 6$ mode, selected as a sample of the multicellular patterns of convection preferred at small Ekman numbers. Three projections of the components of the velocity field (v_r, v_θ, v_ϕ), and the kinetic energy density are displayed in each figure (see figure captions). The contour plots of the temperature perturbation strongly resemble those of the radial velocity, and they are not plotted. The projections in figures 3(a) and 4(a) are taken on spheres of $r = r_i + 0.70d$ and $r = r_i + 0.47d$ for v_r , and $r = r_i + 0.98d$ for the rest, although all of them are plotted at the same size. In this way, all the projections are taken nearly cutting the extrema of every scalar field. The projections on spherical surfaces of smaller radius lose some of the cells extending only to low latitudes. Projections in figures 3(b) and 4(b) are taken on the equatorial plane, and all meridional sections in figures 3(c) and 4(c) are cut more or less by the centre of a v_r vortex. The grey scale is the same for each row of contour plots in each figure. White

means positive components of the velocity field. Notice that $v_\theta = 0$ in the equatorial plane, so the contour lines in figures 3(e) and 4(e) are residuals.

Figure 3 corresponds to the preferred eigenfunction at $E_Z = 1.92 \times 10^{-5}$, $(R_c^4)_Z = 38.90$ of figure 2(c). In Zhang (1993) it is shown that the inertial waves extend to a characteristic latitude $\mathcal{L} = (2/m)^{1/2}$, m being the azimuthal wavenumber. Since this latitude is very small, the presence of an inner sphere is irrelevant for wave motions with $m > \pi(1 + \eta)/2(1 - \eta)$, where η is the radius ratio of the spherical shell. We have measured the extent of the thermal–inertial waves in the equatorial zone following the criterion given for the solutions of the Poincaré equation, i.e. we consider an exponential decrease of the waves with latitude, and look for the latitude \mathcal{L} at which the maximum of v_φ diminishes down to v_φ/e . Numerically, we found $\mathcal{L} = (90^\circ - \theta) \approx 29^\circ$. Although $E = 3.00 \times 10^{-5}$ is not extremely high, the waves are much more confined than the theoretical prediction. In the case of figure 3, theoretically for $m = 4$, $\mathcal{L} = 40.5^\circ$. The discrepancy is probably due to the inclusion of the buoyancy term in our linear analysis.

For $E_Z < 1.9 \times 10^{-5}$, multicellular patterns of convection become preferred. When the Ekman number is decreased, the convection spreads to high latitudes without detaching from the equator. The spiralling flow tends to split, forming a multicellular spiral in the boundary layer. The $m = 6$ tri-cellular pattern found at $E_Z = 3.70 \times 10^{-6}$ is shown in figure 4. In this case, the convection affects up to $(90^\circ - \theta) \approx 44^\circ$, the main Θ cell moves towards the inner boundary. We think that the bi-cellular mode (not shown here) was also found numerically in Zhang (1995) (see his figure 3), but interpreted as the spiralling columnar mode preferred at higher Prandtl numbers.

The meridional sections display the z -dependence of the components of the velocity field. Except in the very thin Ekman boundary layers, v_φ fulfils the Taylor–Proudman constraint, because it is a component orthogonal to the axis of rotation. We have checked that, at high rotation rates, this becomes the strongest component on the spherical surfaces near the outer boundary. In consequence, the contour plots of kinetic energy density of figure 4(j–l) resemble those of v_φ , and the energy is also almost z -independent. The perturbations from bi-dimensionality mainly come from v_r and v_θ .

3.2. Dependence of low-Prandtl-number flows on the Ekman number

In order to study the dependence of the low-Prandtl-number flows on the Ekman number, including the transition between prograde and retrograde modes, $\sigma = 0.1$ has been selected.

Figure 5 displays the results of the linear stability analysis as a function of E (see figure caption). If $E < 10^{-4}$, the regime dominated by the Coriolis force is fully developed, and, in agreement with Zhang (1992) and Yano (1992), prograde SC modes of convection become preferred. So, from this point, the flow remains mono-cellular down to the lowest E values explored. In this case, the vortices detach from the equator when the rotation rate is increased, avoiding the formation of extremely strong Ekman layers near $\theta = \pi/2$, and move towards the inner boundary, i.e. the Ekman layers affect only mid- and high-latitudes. For instance, at $E = 3.78 \times 10^{-5}$, the SC modes have the maximum at $r \approx 0.6r_o$, and the velocity field near the outer surface affects latitudes higher than $(90^\circ - \theta) \approx 13^\circ$. It is important to notice that these values vary a lot with the parameters E , σ , and η .

Out of the asymptotic regime, the neutral stability curves of $|\omega_c^m|$ and ω_c^m versus E (figures 5b, c), show clearly three different types of transition among modes of the same m . For $E > 3.43 \times 10^{-3}$ and $m < 3$, there is a competition between

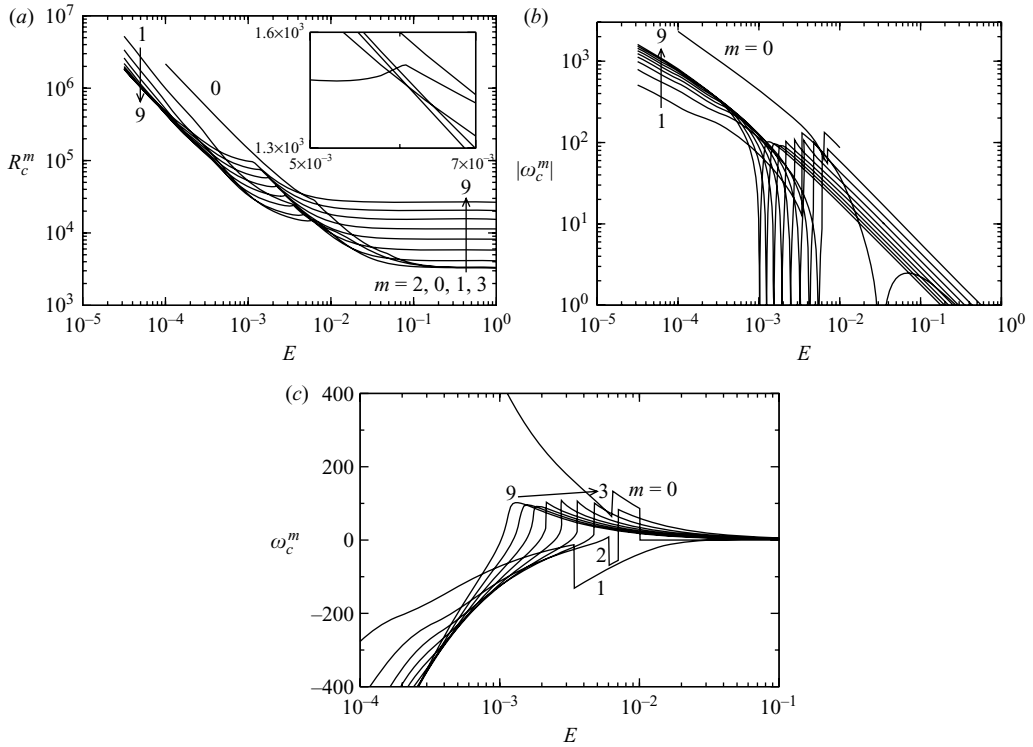


FIGURE 5. (a) The critical Rayleigh number R_c^m , and (b) the critical precession frequency $|\omega_c^m|$, of each critical mode of azimuthal wavenumber m , plotted versus E for $\sigma = 0.1$. (c) Detail of (b) in linear vertical scale showing the jump to spiralling columnar modes of convection.

antisymmetric prograde and symmetric retrograde body modes. The former can also be preferred at the onset of convection, as happens with the $m = 1$ mode in the interval $5.88 \times 10^{-3} < E < 6.10 \times 10^{-3}$, located just before the big cusp of the envelope of figure 5(a) (see also the detail). We have compared the balance of terms of the equations for the preferred antisymmetric mode, and for the neighbouring symmetric solutions of higher and lower E . The only difference found is a slight decrease of the viscous diffusive and buoyancy terms in the antisymmetric modes.

If $m > 3$, only symmetric modes become selected. For $3 \leq m \leq 6$, the cusp of each curve in figure 5(a) is the intersection of two curves of symmetric retrograde modes, although one of them becomes prograde when E is decreased. This change of sign of the precession frequency corresponds to the 'fall' of $|\omega_c^m|$ to zero in figure 5(b). The crossings can also be seen as jumps of ω_c^m in figure 5(c). For $m > 6$, the jumps disappear. To see in detail why this happens, the three lowest neutral stability curves with $m = 5$ and $m = 7$ are plotted in figure 6. The type of line gives the correspondence between the (E, R^m) and (E, ω^m) curves. Moreover, the meaning of the acronyms used in the labels of the curves, and, from now on, in the text is summarized in table 2.

Following the solid curve in figure 6(a) from high to low E values, the body modes of the PS2 curve transform their spatial structure continuously, becoming PS1 modes after the first fold, and NS1 after the second. These NS1 modes are the SC preferred at high rotation rates. The jump of the $m = 5$ critical curve in figure 5(c) is associated to the intersection of the dotted PS1, and the solid NS1 curves at $E = 2.76 \times 10^{-3}$

Acronyms	Symmetry	Sign of ω	Number of latitudinal cells
PS1	Symmetric	Positive (retrograde)	1
PS2	Symmetric	Positive (retrograde)	2
NS1	Symmetric	Negative (prograde)	1
NA1	Antisymmetric	Negative (prograde)	1

TABLE 2. Acronyms for the leading modes found at high Ekman number.

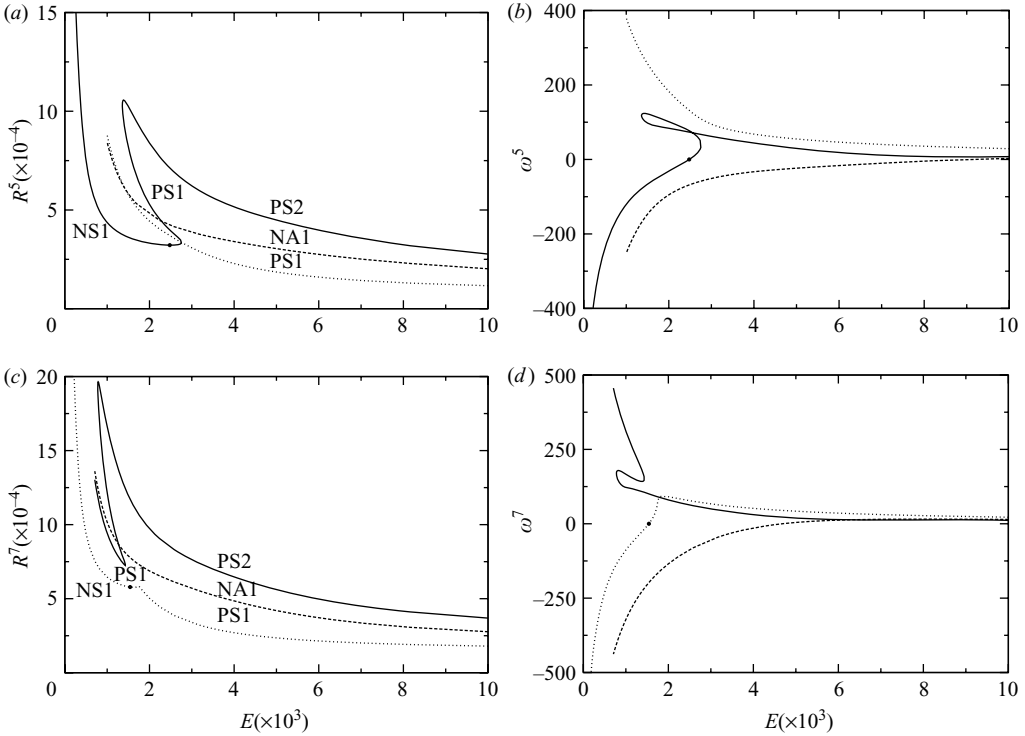


FIGURE 6. (a) The Rayleigh number R^5 , and (b) the precession frequency ω^5 of the three lowest marginal stability curves of azimuthal wavenumber $m = 5$, plotted versus E for $\sigma = 0.1$. (c) R^7 and (d) ω^7 , for the three lowest curves of $m = 7$. The meaning of labels PS1, PS2, NS1, and NA1 is summarized in table 2.

in figure 6(a). Notice that at this point both are mono-cellular symmetric solutions of positive precession frequency (PS1). The change of sign of ω_c takes place at $E = 2.48 \times 10^{-3}$, marked with a full circle in the figure, close to the crossing.

For $m = 7$, there is a qualitative change in the neutral stability curves. By comparing figure 6(a) with figure 6(c) it is easy to recognize an interchange of curves. In figure 6(c), the right-hand part of PS1 remains connected with the left-hand part of NS1, forming the first lower marginal curve, and the left-hand part of PS1 (dotted in figure 6a) remains connected with the first part of NS1, forming the solid line of figure 6(c), which has two very narrow folds. This phenomenology was also described for stress-free boundary conditions in the pioneering numerical work of Zhang & Busse (1987).

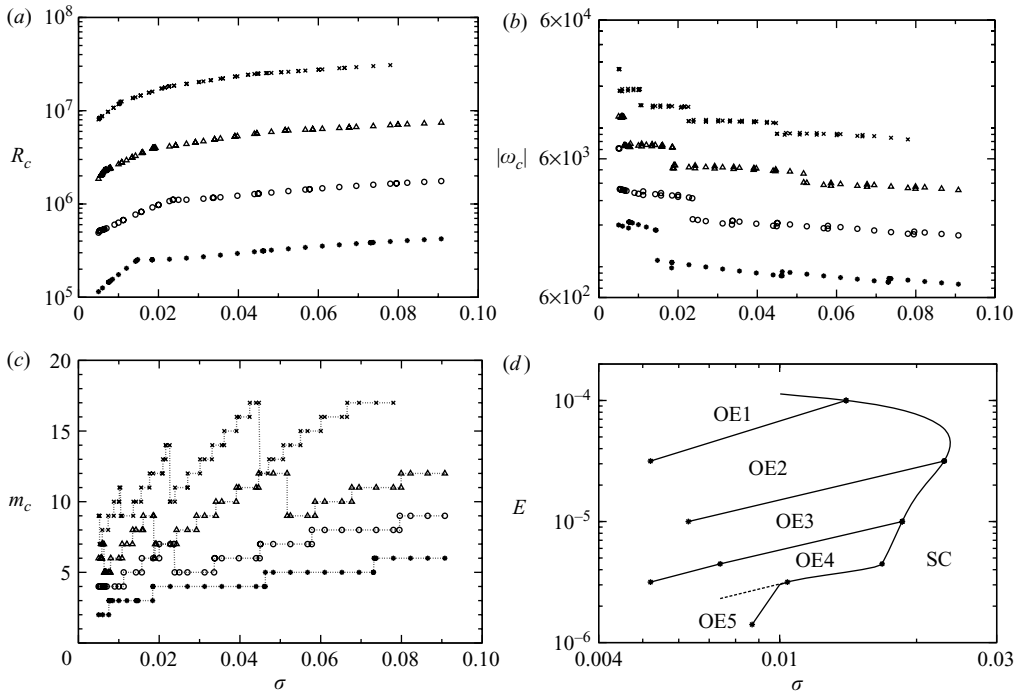


FIGURE 7. (a) The critical Rayleigh number R_c , (b) the critical precession frequency $|\omega_c|$, (c) the critical wavenumber m_c , plotted versus σ . From bottom to top, *, \circ , Δ and \times mean $E = 10^{-4}$, 3.16×10^{-5} , 10^{-5} and 3.16×10^{-6} , respectively (d). The transitions among the different modes of convection. The stars correspond to calculated points.

The interchange of like-parity modes is analysed in detail for the onset of oscillatory binary fluid convection in Batiste *et al.* (1999). According to these authors, the interchange takes place at a resonant double-Hopf bifurcation (surely hidden by the critical non-resonant double-Hopf bifurcations), where the crossing neutral curves become tangent. At this point, both modes will have the same frequency. This explains why along the critical stability curves (like those of $m = 7, 8, 9$ in figure 5c) there are cusps without jumps in the frequency, or abrupt changes in the eigenfunctions. The values of m (3 and 6 in this case) which separate the different behaviours of the neutral curves depend on η . A resonant double-Hopf bifurcation has codimension-three, and to determine the point of tangency without changing m , a third parameter (η or σ) must be moved.

The continuous transformation of the eigenfunctions along the folds of the curves of symmetric modes, and the interaction of modes described, explain why multicellular modes are never preferred at moderate and high σ values. Unlike what happens when $\sigma = 0.005$, for $\sigma = 0.1$ the crossing of the lowest curves with the same m takes place after the transformation, and then, all of them are NS1 (SC). For instance, the mono-cellular $m = 7$ NS1 (SC) mode, which becomes critical at $E \approx 5.77 \times 10^{-5}$, comes from a bi-cellular PS2 mode.

3.3. Prandtl number dependence

In order to study the transition between the OEA and the SC patterns of convection, the envelope of the marginal stability curves (σ, R_c^m) is shown in figure 7(a-c) for four E values in the small Ekman number limit ($3.16 \times 10^{-6} < E < 10^{-4}$). Table 3 gives the

Jump	$E \times 10^5$	σ	$R_c \times 10^{-5}$	$ \omega_c \times 10^{-3}$	m_c
OEA1/OEA2	3.16	0.0052	5.12	7.11/3.63	4/4
OEA2/OEA3	1.00	0.0063	22.4	12.0/7.49	7/5
OEA3/OEA4	0.447	0.0074	66.0	18.2/12.9	9/7
OEA3/OEA4	0.316	0.0052	83.3	26.5/18.6	9/7
OEA1/SC	10.0	0.014	2.47	1.83/1.11	3/3
OEA2/SC	3.16	0.023	11.1	3.12/2.20	7/7
OEA3/SC	1.00	0.0186	39.5	7.25/5.14	9/6
OEA4/SC	0.447	0.0168	101.6	12.6/9.56	11/8
OEA4/SC	0.316	0.0104	120.0	19.1/14.6	11/9
OEA5/SC	0.141	0.0087	306.0	34.9/27.8	13/11
SC/SC	1.00	0.051	61.4	4.69/4.05	12/9
SC/SC	0.316	0.023	182.0	14.2/11.2	14/10
SC/SC	0.316	0.045	250.0	10.8/9.09	17/12

TABLE 3. Parameters and critical values of the bi-critical points of figure 7 giving rise to jumps of decreasing $|\omega_c|$. The number after OEA indicates the number of latitudinal cells near the outer boundary.

parameters and features of the bi-critical points where changes of types of preferred eigenfunctions (not just changes of m) take place. The table contains additional points calculated for $E = 4.47 \times 10^{-6}$ and $E = 1.41 \times 10^{-6}$ without rounding off new curves up to $\sigma = 0.1$. Figure 7(d) shows the transitions of the table. From the double-Hopf OEA/SC bifurcation, the SC modes detach from the equator, moving towards a cylindrical radius $r \in (r_i, r_o)$, while the OEA modes remain equatorially trapped when σ decreases.

Figure 7(b) shows small increasing, and big decreasing jumps in $|\omega_c|$. The small correspond either to jumps between OEA modes of the same number of latitudinal cells, or between SC modes. In both cases, m_c increases in one unit. This is the normal situation. In contrast, the big jumps are due either to jumps between OEA modes of different numbers of latitudinal cells, between OEA and SC modes, or between SC modes of decreasing m_c (see figure 7c). In order to help to follow them, the discrete points are joined with a dotted line.

Figure 7(d) shows that there is a direct transition between the equatorially trapped (OEA1) and SC modes only near $E = 10^{-4}$, i.e. just at the beginning of the small Ekman number limit. For lower E , the transition is direct from multicellular to SC modes. Moreover, we have been unable to find any simple law defining the OEA/SC transition with non-slip boundaries, unlike in Ardes *et al.* (1997) for stress-free boundary conditions.

At moderate E , the OEA/SC transition occurs near the Prandtl number of some usual experimental fluids, namely for $\sigma < 0.023$. This result agrees with the experimental results of Aubert *et al.* (2001) for liquid gallium ($\sigma = 0.027$). They suggest that the nonlinear flows keep traces of the SC Rossby waves for Ekman numbers of order 10^{-7} , in a spherical shell of $\eta = 0.35$. The location of the transition point can also explain why Zhang & Liao (2004) found OEA critical modes for $\sigma = 0.023$, a very small η , and E order 10^{-6} . Near the OEA/SC transition, a small variation of the parameters and/or the boundary conditions can vary the type of preferred eigenfunction.

In order to understand the jumps among SC modes of decreasing m (see figure 7c), and why the eigenfunctions after the jumps still have the same structure, the two

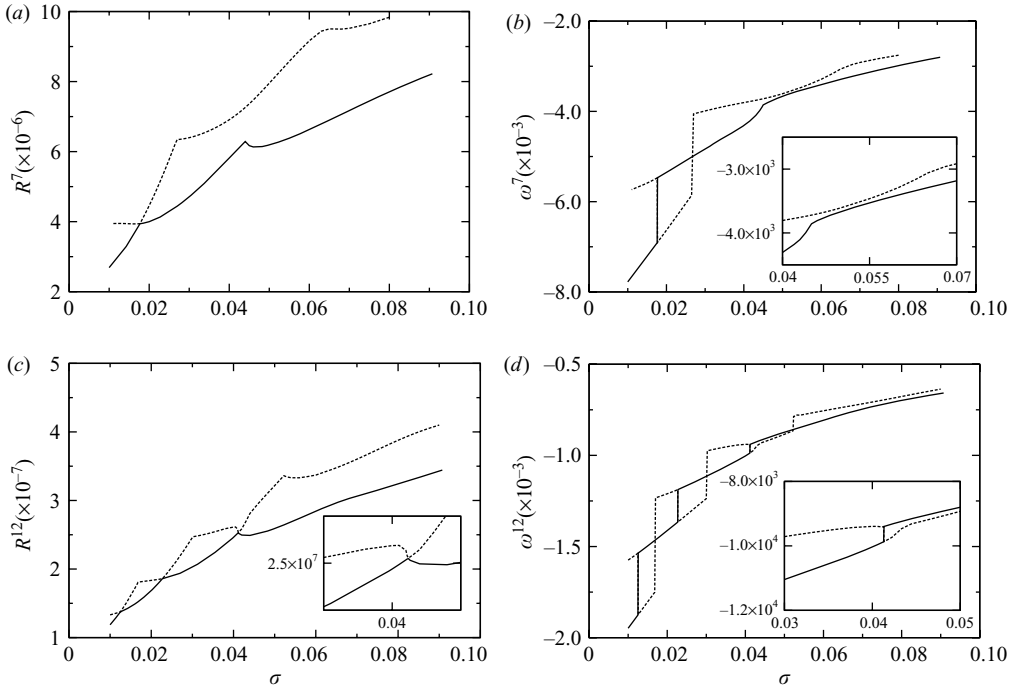


FIGURE 8. (a, c) The Rayleigh number R^7 , and R^{12} , and (b, d) the precession frequencies ω^7 , and ω^{12} , respectively, of the two lowest envelopes of the neutral stability curves of $m=7$, and $m=12$, plotted versus σ , for $E=1 \times 10^{-5}$ and $E=3.16 \times 10^{-6}$, respectively. The solid lines give R_c^m , and the dashed lines correspond to the second mode which becomes linearly unstable.

lowest envelopes of the neutral curves with $m=7$ for $E=10^{-5}$, and $m=12$ for $E=3.16 \times 10^{-6}$ are plotted in figure 8 as functions of σ . Figure 8(a) shows that the solid curve develops a cusp, and the dashed line a bump, near $\sigma=0.043$. This causes an abrupt decrease of R^7 along the solid line for larger σ . The frequency curves of figure 8(b) also become distorted (see detail), becoming nearly tangent close to $\sigma=0.05$. We have checked that other curves of low m have the same behaviour. In contrast, figures 8(c) and 8(d) show the shape of the curves for higher m . It can be seen that close to $\sigma=0.04$, the two curves have already reconnected in the way explained in § 3.2. The details in figures 8(c) and 8(d) show traces of the fold developed by one of the curves before becoming tangent, and the almost equal frequencies of both modes after the bifurcation.

Since for $\sigma > 0.023$ the neutral stability curves are more or less folded, the different degree of deformation of the curves depending on m , mean that curves of low m dominate suddenly again, after others of higher m . This explains the fall of m_c and $|\omega_c|$ in figures 7(b) and 7(c) at the SC/SC jumps. In addition, at the resonant double-Hopf bifurcations, neutral curves of the same m interchange their properties, and then when this m reappears as preferred (in a non-resonant double-Hopf bifurcation) the same structure is seen again along the critical stability curve. In this case, for a given m , it is possible to capture the resonant double-Hopf bifurcation by moving η and/or E , in addition to σ .

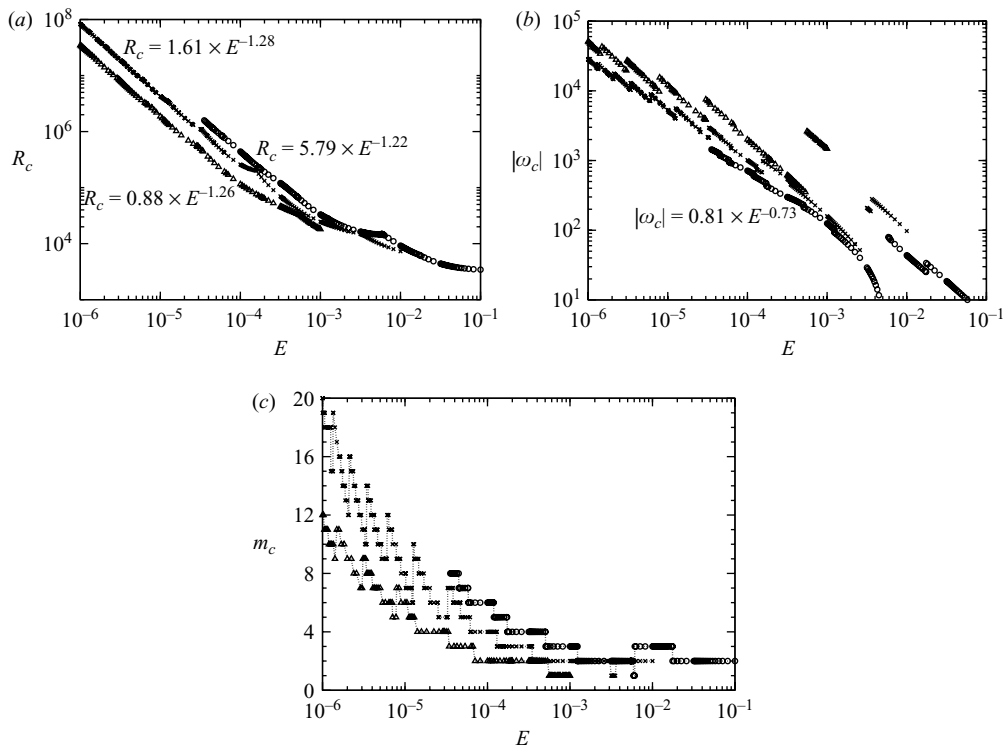


FIGURE 9. (a) The critical Rayleigh number R_c , (b) the corresponding precession frequency $|\omega_c|$, and (c) the critical azimuthal wavenumber m_c versus E . The labels near the curves give the power laws estimated from the numerical results. The symbols Δ , \times and \circ indicate $\sigma = 0.005, 0.025$ and 0.1 , respectively.

3.4. The asymptotic limit

Figure 9 shows the critical Rayleigh number R_c , the precession frequency $|\omega_c|$, and the critical wavenumber m_c versus E , for the two fluids studied in §3.1 and §3.2 (see figure caption). For completeness, we include the results of the linear stability analysis of a fluid of $\sigma = 0.025$ (mercury/liquid gallium), which, in addition of being near the OEA/SC border, has experimental interest in magnetohydrodynamics. To study this transition experimentally it is also worth mentioning the usefulness of the liquid sodium. With $\sigma = 0.01$, it is below the critical value $\sigma = 0.023$, but still near the competition between OEA/SC modes at lower E (see figure 7d).

For $\sigma = 0.025$, and high E values, the critical waves have $\omega_c > 0$, but the antisymmetric $m = 1$ mode with $\omega_c < 0$ is preferred in $3.13 \times 10^{-3} < E < 3.63 \times 10^{-3}$. According to the preceding results, the preferred patterns of convection of fluids with $\sigma \approx 0.023$ can be either OEA or SC modes depending on E . For $E \approx 4.47 \times 10^{-5}$, it is difficult to distinguish from the contour plots the type of preferred eigenfunction. In fact, to decide it, it is necessary to know its position in the (σ, R_c) -plane of figure 7. For $E < 3.16 \times 10^{-5}$, all the critical patterns are SC.

In figure 9(a), the power laws of the numerical fittings for low E are included in our non-dimensional units. The intervals used for the fitting, and the maximal numerical relative errors due to the numerical truncation of the data of figure 9 are given in table 4. They are estimated by recomputing the points with 70 radial, and 110

σ	Interval ($E \times 10^4$)	$E \times 10^5$	ε_{R_c} (%)	ε_{ω_c} (%)
0.1	(0.35, 1)	3.500	2.5×10^{-5}	2.1×10^{-3}
0.025	(0.01, 0.1)	0.100	5.0×10^{-1}	8.6×10^{-2}
0.005	(0.01, 0.1)	0.316	7.8×10^{-2}	9.7×10^{-3}
0.005	(0.01, 0.1)	0.112	2.6	2.6×10^{-1}
0.005	(0.01, 0.1)	0.100	2.9	3.4×10^{-1}

TABLE 4. Prandtl number, interval considered for adjusting the asymptotic laws of figure 9, E of the point in the interval at which the error due to truncation is maximal, and the corresponding numerical relative errors ($\varepsilon\%$) of R_c and ω_c .

latitudinal points. In general, an over-truncation overestimates R_c and underestimates ω_c . However, as can be seen in the table, we have relative errors below 3% for R_c with $\sigma = 0.005$ and $E \approx 10^{-6}$. With these values, the estimated error for the exponent of the power law of R_c is 1.3%, and 17% for the prefactor. For $\sigma = 0.025$, 60 radial and 100 latitudinal points are used everywhere, so the error of the exponent is less than 0.2%, and that of the prefactor is 1.7%. For $\sigma = 0.1$, the truncation error is even smaller, because the curve is cut at higher E .

In any case, the power of R_c is not far from $-4/3$, the leading order of the asymptotic expansions of Roberts (1968), Busse (1970), and Dormy *et al.* (2004) (see §1) for moderate Prandtl numbers. In contrast, the dependence of $|\omega_c|$ on E is not so clear. For $\sigma = 0.005$, the precession frequency diminishes sharply when a new pattern of convection is selected, but keeping the previous slope (see figure 9b). The jumps are smaller as E is decreased. Perhaps this indicates that for ω , the asymptotic limit is not fully reached. Although the fitting of each straight segment gives approximately a 1.10 power, greatly exceeding $-2/3$ given by the asymptotic limits, the law $|\omega_c| = 5.33 \times E^{-0.66}$ is found by considering the interval $10^{-6} < E < 10^{-5}$. The jumps for $E \leq 3.0 \times 10^{-5}$ along this curve are between OEA modes. By increasing σ , the height of the jumps in the same range of E is smaller. For $\sigma = 0.025$ and $E < 4.47 \times 10^{-5}$, there are some E for which it is difficult to classify the eigenfunctions. As in the preceding case, the fitting for $E < 10^{-5}$ gives $|\omega_c| = 2.12 \times E^{-0.68}$. Finally for $\sigma = 0.1$, the power-law dependence of $|\omega_c|$ is included, since for $E < 4.47 \times 10^{-3}$, the dominant modes correspond to the same pattern of eigenfunctions (SC), and the small jumps of increasing $|\omega_c|$ correspond to changes of increasing m_c .

The dependence of m_c on E is plotted in figure 9(c). Again, the discrete points are joined with a dotted lined. By neglecting the discontinuities, we have checked that the potential law $m_c \sim E^{-1/3}$ of the theoretical expansions also fits well to our numerical values. We have found $m_c = 0.15 \times E^{-0.31}$ for $\sigma = 0.005$, $m_c = 0.16 \times E^{-0.34}$ for $\sigma = 0.025$, both for $E < 10^{-5}$, and $m_c = 0.30 \times E^{-0.32}$ for $\sigma = 0.1$ and $E < 10^{-4}$.

4. Concluding remarks

The detailed numerical computations of this work clarify previous results, and also show some unexpected aspects of the thermal convection at low Prandtl numbers, σ .

Far from the small-Ekman-number limit ($E > 3.16 \times 10^{-3}$), the antisymmetric prograde waves with low m_c can be preferred; m_c depending on η . For instance, $m_c = 1$ for $\eta = 0.2$, and in other computations with $\eta = 0.35$ and differential heating (not displayed here), $m_c = 2$.

For $\eta = 0.2$, and a wide range of E (see table 3), the transition OEA/SC takes place near $\sigma = 0.023$, namely, it occurs near the Prandtl number of the experimental liquid metals in normal laboratory conditions. At this value, both modes become unstable almost at once, and consequently nonlinear chaotic dynamics may be expected at or near R_c . So, the numerical and experimental study of these regimes appears as an interesting objective which should be easy to reach in the near future. By decreasing E , the transition to SC modes takes place at lower σ values, this means that at the very low Ekman numbers of the planetary cores, it is very unlikely that convection can excite the outer equatorially attached modes. However, they could be excited by other mechanisms, or become relevant owing to the action of the magnetic field on the equatorial waves.

The location of the transition point could explain why Simitev & Busse (2003) detect temporal-chaotic states near the onset of convection with $\eta = 0.4$ and $\sigma = 0.025$, and a transition to stable travelling waves followed by amplitude vacillations for moderate and large σ values. However, the nonlinear results of Schnaubelt & Busse (1992), Herrmann & Busse (1997), Pino *et al.* (2001) and Plaut & Busse (2002) among others, obtained for cylindrical annuli of large radius ratios, suggest that in thin spherical shells, the preceding behaviour could have another reason. Sideband instabilities leading to spatially modulated waves, and mean zonal flow/resonance instabilities at moderate/low σ are the mechanisms responsible for the instability of the thermal Rossby waves. At low σ , the region of stability of the waves comes away from the neutral stability curve, and becomes narrower until disappearing for very low σ values, so stable complex time-dependent flows develop at the onset of convection.

Our results are restricted to wide spherical shells, and it could be interesting (but very expensive) to see how the transition OEA/SC moves by narrowing the gap. Other linear calculations made for $\eta = 0.35$ down to $E = 1.20 \times 10^{-7}$ with differential heating, show that the dominant modes in the small-Ekman-number limit are also columnar for $\sigma = 0.1$, but attached to the inner boundary.

For σ greater than approximately 0.023, the modulation of the eigenfunctions along the folds of the neutral stability curves (σ, R^m) explains the bi-critical bifurcations labelled SC/SC. When two neutral stability curves become tangent, the eigenfunctions at the tangency point have the same structure. Moreover, a sudden decrease in the Rayleigh number takes place (see figure 8). Consequently, if a neutral curve becomes preferred after the tangency, at a higher σ , the new preferred modes look like those that were preferred before (but for the azimuthal wavenumber).

For very low σ , the equatorially trapped mono-cellular modes are soon superseded by multicellular modes when E decreases. Therefore, a direct transition between equatorially trapped and spiralling columnar modes exists only in a narrow range of Ekman numbers, at the beginning of the rapidly rotating regime. This result agrees qualitatively with the sketch of Plaut & Busse (2005). They also found that, in rotating annuli, at low E and σ the transition is between multicellular and spiralling columnar modes. The z -dependence of the modes of convection inside the fluid shell is stronger in spherical than in cylindrical geometry. When the multicellular patterns become selected, the convection tends to fill the shell, spiralling from the body of the fluid by the effect of the rotation, but without detaching from the outer equatorial boundary. At the same time, small vortices, which remain stuck to the outer boundary, appear. By comparing the structure of these modes with those found by Ardes *et al.* (1997), and Zhang & Liao (2004) with stress-free boundary conditions, it seems that the non-slip boundaries tend to inhibit the formation of such vortices, in the sense that they are smaller and more confined.

The numerical potential laws obtained with non-slip boundary conditions and low Prandtl numbers agree well on average with the leading order of the theoretical asymptotic expansions of Roberts (1968), Busse (1970) and Dormy *et al.* (2004). However, the jumps of the precession frequencies, for low σ values, can indicate that even at $E = 10^{-6}$ the asymptotic limit for ω_c is not fully reached.

This work is supported by Spain MEC-DGI, and Catalonia GENCAT under grants FIS2004-01066 and 2005SGR01028, respectively. We thank Professor F. H. Busse and anonymous referees for their useful comments and suggestions.

REFERENCES

- AL-SHAMALI, F., HEIMPEL, M. & ARNOU, J. 2004 Varying the spherical shell geometry in rotating thermal convection. *Geophys. Astrophys. Fluid Dyn.* **98**, 153–169.
- ARDES, M., BUSSE, F. H. & WICHT, J. 1997 Thermal convection in rotating spherical shells. *PEPI* **99**, 55–67.
- AUBERT, J., BRITO, D., NATAF, H.-C., CARDIN, P. & MASSON, J. P. 2001 A systematic experimental study of rapidly rotating spherical convection in water and liquid gallium. *Phys. Earth Planet. Inter.* **128**, 51–74.
- BATISTE, O., MERCADER, I., NET, M. & KNOBLOCH, E. 1999 Onset of oscillatory binary fluid convection in finite containers. *PRE* **59**, 6730–6741.
- BUSSE, F. H. 1970 Thermal instabilities in rapidly rotating systems. *J. Fluid Mech.* **44**, 441–460.
- BUSSE, F. H. & SIMITEV, R. 2004 Inertial convection in rotating fluid spheres. *J. Fluid Mech.* **498**, 23–30.
- DORMY, E., SOWARD, A. M., JONES, C. A., JAULT, D. & CARDIN, P. 2004 The onset of thermal convection in rotating spherical shells. *J. Fluid Mech.* **501**, 43–70.
- ECKE, R. E., ZHONG, F. & KNOBLOCH, E. 1992 Hopf bifurcation with broken reflection symmetry in rotating Rayleigh–Bénard convection. *Europhys. Lett.* **19**, 177–182.
- FINLAY, C. C. & JACKSON, A. 2003 Equatorially dominated magnetic field change at the surface of the Earth's core. *Science* **300** (5628), 2084–2086.
- GILLET, N., BRITO, D., JAULT, D. & NATAF, H.-C. 2007 Experimental and numerical studies of convection in a rapidly rotating spherical shell. *J. Fluid Mech.* **580**, 83–121.
- HERRMANN, J. & BUSSE, F. H. 1997 Convection in a rotating cylindrical annulus. Part 4. Modulations and transitions to chaos at low Prandtl numbers. *J. Fluid Mech.* **350**, 209–229.
- JALETZKY, M. 1999 Experimental study of rotating cylindrical annulus convection. PhD thesis, University of Bayreuth.
- JONES, C. A., SOWARD, A. M. & MUSSA, A. I. 2000 The onset of thermal convection in a rapidly rotating sphere. *J. Fluid Mech.* **405**, 157–179.
- LEHOUCQ, R. B., SORENSSEN, D. C. & YANG, C. 1998 *ARPACK User's Guide: Solution of Large-Scale Eigenvalue Problems with Implicitly Restarted Arnoldi Methods*. SIAM.
- LI, L., ZHANG, P., LIAO, X. & ZHANG, K. 2005 Multiplicity of nonlinear thermal convection in a spherical shell. *Phys. Rev. E* **71**, 016301(1)–016301(9).
- PINO, D., MERCADER, I. & NET, M. 2000 Thermal and inertial modes of convection in a rapidly rotating annulus. *Phys. Rev. E* **61**, 1507–1517.
- PINO, D., NET, M., SÁNCHEZ, J. & MERCADER, I. 2001 Thermal Rossby waves in a rotating annulus: their stability. *Phys. Rev. E* **63**, 056312(1)–056312(14).
- PLAUT, E. & BUSSE, F. H. 2002 Low-Prandtl-number convection in a rotating annulus. *J. Fluid Mech.* **464**, 345–363.
- PLAUT, E. & BUSSE, F. H. 2005 Multicellular convection in rotating annuli. *J. Fluid Mech.* **528**, 119–133.
- ROBERTS, P. H. 1968 On the thermal instability of a rotating fluid sphere containing heat sources. *Phil. Trans. R. Soc. Lond. A* **263**, 93–117.
- SCHNAUBELT, M. & BUSSE, F. H. 1992 Convection in a rotating cylindrical annulus. Part 3. Vacillating and spatially modulated flow. *J. Fluid Mech.* **245**, 155–173.

- SECCO, R. A. & SCHLOESSIN, H. H. 1989 The electrical resistivity of solid and liquid Fe at pressures up to 7 GPa. *J. Geophys. Res. B* **94**, 5887–5894.
- SIMITEV, R. & BUSSE, F. H. 2003 Patterns of convection in rotating spherical shells. *New J. Phys.* **5**, 97.1–97.20.
- SOWARD, A. M. 1977 On the finite amplitude thermal instability in a rapidly rotating fluid sphere. *Geophys. Astrophys. Fluid Dyn.* **9**, 19–74.
- WIJS, G. A. D., KRESSE, G., VOČADLO, L., DOBSON, D., ALFÈ, D., GILLAN, M. J. & PRICE, G. D. 1998 The viscosity of liquid iron at the physical conditions of the Earth's core. *Nature* **392**, 805–807.
- YANO, J. I. 1992 Asymptotic theory of thermal convection in a rapidly rotating system. *J. Fluid Mech.* **243**, 103–131.
- ZHANG, K. 1992 Spiralling columnar convection in rapidly rotating spherical fluid shells. *J. Fluid Mech.* **236**, 535–556.
- ZHANG, K. 1993 On equatorially trapped boundary inertial waves. *J. Fluid Mech.* **248**, 203–217.
- ZHANG, K. 1994 On coupling between the Poincaré equation and the heat equation. *J. Fluid Mech.* **268**, 211–229.
- ZHANG, K. 1995 On coupling between the Poincaré equation and the heat equation: non-slip boundary condition. *J. Fluid Mech.* **284**, 239–256.
- ZHANG, K. & BUSSE, F. H. 1987 On the onset of convection in rotating spherical shells. *Geophys. Astrophys. Fluid Dyn.* **39**, 119–147.
- ZHANG, K. & JONES, C. A. 1993 The influence of Ekman boundary layers on rotating convection. *Geophys. Astrophys. Fluid Dyn.* **71**, 145–162.
- ZHANG, K. & LIAO, X. 2004 A new asymptotic method for the analysis of convection in a rapidly rotating sphere. *J. Fluid Mech.* **518**, 319–346.
- ZHANG, K., LIAO, X. & BUSSE, F. 2007 Asymptotic solutions of convection in rapidly rotating non-slip spheres. *J. Fluid Mech.* **578**, 371–380.